



Solar Energetic Particles Produced during Two Fast Coronal Mass Ejections

Xiaolei Li¹ , Yuming Wang^{1,2,3} , Jingnan Guo^{1,2} , and Shaoyu Lyu¹ ¹ CAS Key Laboratory of Geospace Environment, Department of Geophysics and Planetary Sciences, University of Science and Technology of China, Hefei 230026, People's Republic of China; ymwang@ustc.edu.cn² CAS Center for Excellence in Comparative Planetology, University of Science and Technology of China, Hefei 230026, People's Republic of China³ Mengcheng National Geophysical Observatory, University of Science and Technology of China, Mengcheng 233527, People's Republic of China

Received 2022 January 29; revised 2022 March 6; accepted 2022 March 7; published 2022 March 21

Abstract

Two recent extremely fast coronal mass ejections (CMEs) are of particular interest. The first one originated from the southern hemisphere on 2021 October 28 and caused strong solar energetic particle (SEP) events over a wide longitude range from Earth, STEREO-A, to Mars. However, the other one, originating from the center of the Earth-viewed solar disk 5 days later, left weak SEP signatures in the heliosphere. Based on the white-light images of the CMEs from the Solar and Heliospheric Observatory (SOHO) and the Ahead Solar Terrestrial Relations Observatory (STEREO-A), in combination with the observations of the corresponding solar flares, radio bursts, and in situ magnetic fields and particles, we try to analyze the series of solar eruptions during October 28–November 2 as well as their correspondences with the in situ features. It is found that the difference in SEP features between the two CMEs is mainly due to (1) the seed particles probably supplied by associated flares and (2) the magnetic connection influenced by the preceding solar wind speed.

Unified Astronomy Thesaurus concepts: Solar coronal mass ejections (310); Solar energetic particles (1491); Solar flares (1496)

Supporting material: animation

1. Introduction

Space radiation induced by solar energetic particles (SEPs) associated with solar eruptions may potentially endanger human bodies and equipment in space and at high altitudes near Earth. SEPs can mainly be accelerated by two different physical mechanisms: magnetic reconnection acceleration and shock-wave acceleration (Reames 2013, 2020). Acceleration by magnetic reconnection during the solar flares or jets often leads to impulsive and narrow-spread ($\lesssim 40^\circ$) SEP events (Reames 1999; Cane et al. 2002; Buřík 2020). Magnetic flux ropes can be generated at the Sun and may erupt out as coronal mass ejections (CMEs). Fast CMEs can drive shock waves ahead, which continue accelerating particles upstream, thus leading to large gradual long-term SEP events.

The gradual SEP intensities generally have a positive correlation with the CME speeds, but not all of the fast CMEs correspond to the high peak flux of high-energy SEPs (Kahler & Vourlidas 2005; Shen et al. 2007; Kihara et al. 2020). There are four main factors causing the absence of high-energetic particles (>20 MeV) (Lario et al. 2020), including (1) no magnetic connection between the source of the particles and the observer, (2) CME too slow or too narrow to drive a strong shock, (3) lack of pre-CME seed particles, and (4) lack of particles accelerated into space by CME-associated flares. The strongest particle acceleration often occurs near the nose of a shock, which generally travels with the highest speed, resulting in the highest peak flux when the observer has the best magnetic connectivity to the shock nose (e.g., Xie et al. 2019; Kihara et al. 2020). Due to the differences in the characteristics of the shock and upstream solar wind at different regions of the

shock, the SEP events associated with the same shock can behave differently for observers at different locations (e.g., Reames 2010; Rouillard et al. 2011; Zhuang et al. 2022).

From October 28 until November 2 in 2021, there were eight CMEs observed by the coronagraphs of the Large Angle and Spectrometric Coronagraph (LASCO) (Brueckner et al. 1995) on board the Solar and Heliospheric Observatory (SOHO) and the Sun Earth Connection Coronal and Heliospheric Investigation (SECCHI) (Howard et al. 2008) on board the Ahead Solar Terrestrial Relations Observatory (STEREO-A). Two of them, viewed as halo CMEs from Earth, are extremely fast and wide, with their front velocity above 1200 km s^{-1} . At Earth, STEREO-A, and Mars, which were separated by 37° (the first two) and 154° (the last two) in the heliospheric longitude (see Figure 1(b) for details), we observed the arrival of intense high-energy SEPs from the first CME on October 28, but poor energetic particle signatures from the other one on November 2. According to the reconstruction of the two CMEs, we find that they both have similar speeds, sizes, and longitudinal propagating directions, and the second is even closer to the ecliptic plane than the first one. Why are their energetic particle features so different? Motivated by this question, we analyze the remote-sensing observations of the eight CMEs (Section 2) and the corresponding in situ observations at Earth, STEREO-A, and Mars (Section 3). The discussion and summary are given in Section 4.

2. Remote-sensing Observations of the CMEs from October 28 to November 2 in 2021

We analyze the remote-sensing data from SOHO, the Solar Dynamics Observatory (SDO), and the Geostationary Operational Environmental Satellites (GOES) spacecraft near Earth as well as from STEREO-A located 0.96 au from the Sun 37°

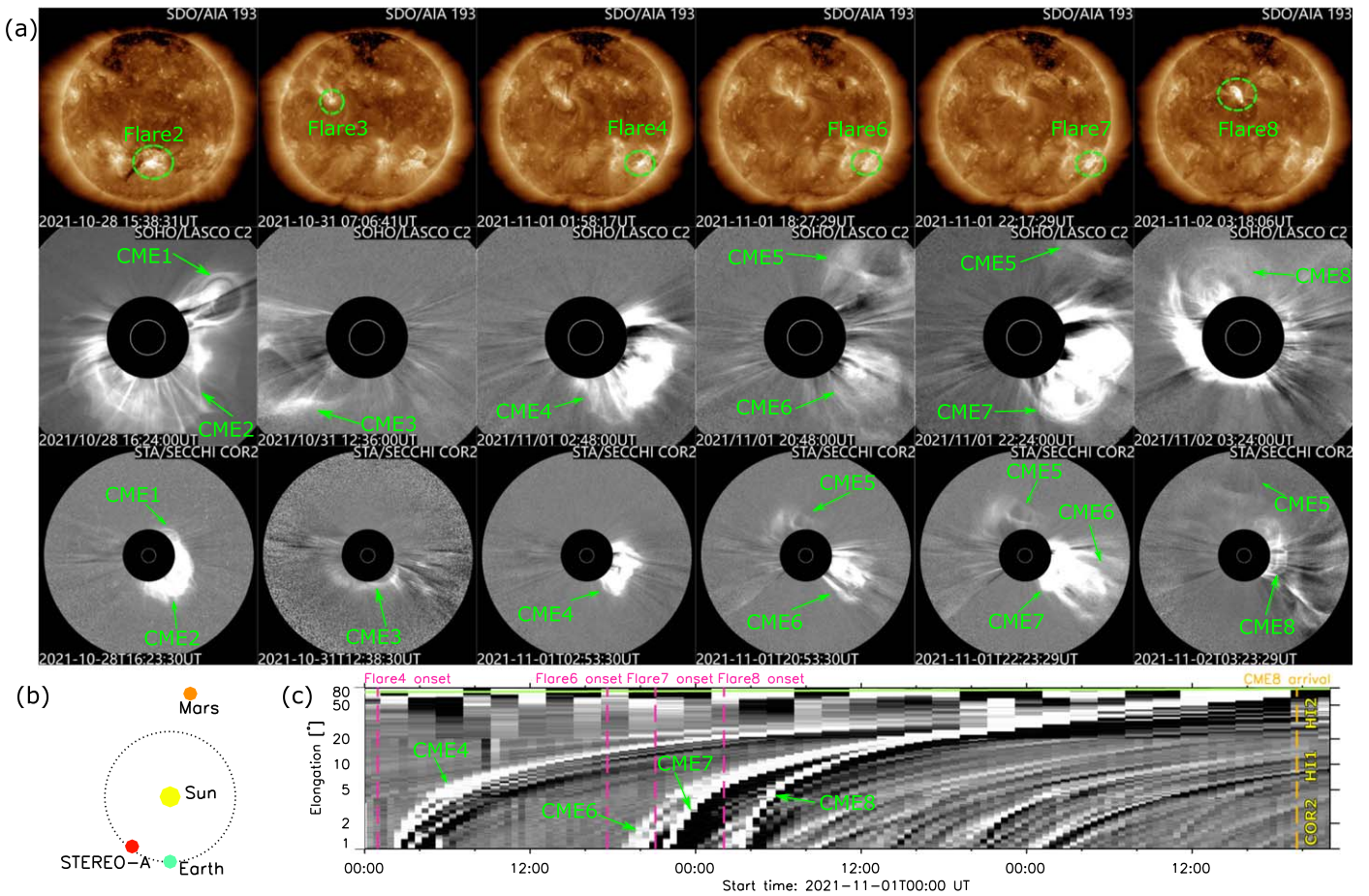


Figure 1. Observations of eight CMEs between 2021 October 28 and November 2. (a) Remote-sensing observations of eight CMEs and their associated flares. First row: SDO/AIA193 images of the flares (marked by the green dashed oval). Second row: preprocessed base-difference SOHO/LASCO C2 images of the CMEs. Third row: preprocessed base-difference STEREO-A/SECCHI COR2 images of the CMEs. (b) Positions of the Sun (big yellow dot), STEREO-A (red dot), Earth (green dot with its orbit shown as the dotted circle), and Mars (orange dot) on the ecliptic plane on 2021 October 29 00:00 UT. (c) The time–elongation plot for the STEREO-A COR2, H11, and H12 running-difference images along the position angle of 264° where Earth is located. The front of CMEs 4, 6, 7, and 8 and the trace of Earth (green curve) are marked. The corresponding CME’s flare-onset time (magenta dashed line) and CME-driven shock arrival time (orange dash line) are marked as well.

east of Earth. Their positions in the heliosphere on 2021 October 29 are shown in Figure 1(b).

(Eyles et al. 2009) running-difference images along the position angle of 264° where Earth is located.

2.1. CMEs in the White-light Images of Coronagraph and Heliospheric Imagers

From October 28 to November 2, we find eight typical CMEs that occurred in the field of view of both SOHO/LASCO C2 and STEREO-A/SECCHI COR2 coronagraph images and name them CME 1 to CME 8 chronologically according to t_{C2} , which is defined as their time of first appearance in SOHO/LASCO C2 images (see the second and third rows of Figure 1(a) for the C2 and COR2 images of the eight CMEs). As Figure 1(a) shows, from the perspective of Earth, after 15:00 UT on October 28, CME 1 erupted as a limb CME at the northwest and CME 2 erupted later as a halo CME. Two days later, CME 3 propagated out toward the east. On November 1, except for CME 5 as a northwest limb CME, CMEs 4, 6, and 7 were launched from the west limb in sequence and CME 7 caught up with CME 6 the next day. On November 2, CME 8, another halo CME, first entered the field of view of LASCO C2 at 02:48 UT and caught up with CME 7 around 14:00 UT. CME 8 finally caught up with CME 4 at around 2:00 UT on November 3. These CME–CME interactions are identified from the time–elongation map of STEREO-A/SECCHI COR2 and Heliospheric imagers 1 and 2

2.2. CMEs’ Corresponding Solar Flares

We check the corresponding flare events before the CME eruption based on extreme ultraviolet imaging observations by the Atmospheric Imaging Assembly (AIA) (Lemen et al. 2012) on board SDO. Except for CME 1 and CME 5 at the west limb, which are probably related to backside flare events seen from Earth, we find suitable solar flare events for the other CMEs on the solar disk and name them Flare 2 to Flare 8 accordingly (see the first row of Figure 1(a) for Flares 2, 3, 4, 6, 7, and 8 corresponding to CMEs 2, 3, 4, 6, 7, and 8, respectively).

We search through measurement data from the X-Ray Sensor (XRS) (Chamberlin et al. 2009) on board National Oceanic and Atmospheric Administration (NOAA) GOSE-17 (see the top panel of Figure 3) for the flare-onset time t_f , location on the solar disk, and their classes (see Table 1 for details). For the six eruption flares at the front side of the solar disk, Flares 2, 4, 6, and 7 are located at active region 12887 in the southern hemisphere while the other two (Flare 3 and Flare 8) are at active region 12891 in the northern hemisphere. Flare 2 reaches X1.0 class while Flare 4 and Flare 8, each at the class of M1.5 and M1.6, respectively, are weaker. The other three are

Table 1
Observable Characteristics of the Eight CMEs from October 28 to November 2

No.	CMEs ^a						Associated Flares			Type III Radio Burst		Comments				
	t_{C2} (UT)	Direction	γ ($^{\circ}$)	δ ($^{\circ}$)	κ	v_n (km s^{-1})	t_f^b (UT)	Loc	Class	~ 1 MHz Duration		Magnetic Connection ^c			Shock Arrival ^d	
										STA	Earth	Mars	STA	Earth	STA (UT)	Earth (UT)
1	2021 Oct 28 13:48	N28W105	3.0	23.0	0.23	467 ± 10	...	Backside	N	N	N
2	2021 Oct 28 15:48	S26W00	-28.5	89.0	0.96	1362 ± 13	15:17	S28W02(AR12887)	X1.0	35 min	32 min	Y	Y	Y	Oct 30 12:22	Oct 31 09:33
3	2021 Oct 31 08:54	S07E46	-5.0	40.0	0.25	470 ± 35	06:53	N16E25(AR12891)	C3.0	2 min	<1 min	N	N	N	Nov 03 09:36	...
4	2021 Nov 01 02:00	S18W26	21.2	75.5	0.80	679 ± 29	00:57	S28W46(AR12887)	M1.5	29 min	28 min	N	Y	Y	?	?
5	2021 Nov 01 12:24	N20W155	-39.1	14.5	0.21	306 ± 7	...	Backside	N	N	N
6	2021 Nov 01 18:24	S23W40	-15.7	16.5	0.48	558 ± 7	17:36	S30W56(AR12887)	C1.3	4 min	<1 min	N	Y?	Y?
7	2021 Nov 01 21:36	S20W53	38.6	31.3	0.49	1014 ± 35	21:05	S30W70(AR12887)	C4.1	6 min	5 min	N	N	Y?
8	2021 Nov 02 02:48	N20E09	-48.6	35.2	0.87	1235 ± 35	02:03	N20E02(AR12891)	M1.6	6 min	4 min	N	Y	Y?	Nov 04 04:15	Nov 03 19:36

Notes.

^a t_{C2} is the time when the CME first occurred in the SOHO/LASCO C2 images. γ , δ , and κ represent the tilt angle of the flux rope to the longitudinal direction, the half-angle of the flux rope axis, and the sine of the half-angle of the cone at the flux rope foot, respectively.

^b t_f is the onset time of the associated flare.

^c Y or N means good or poor magnetic connection between the CME front and the observer. The question mark means the in situ observed poor high-energy (>20 MeV) SEP signature despite a good magnetic connection.

^d The question mark here means the shock propagated to the observer but was undetected by in situ observation.

C-class flares. The magnetic reconnection was likely much more efficient during Flare 2 than that during Flare 8, leading to more energetic particles accelerated and released via CME 2/Flare 2.

2.3. CMEs' Corresponding Type III Radio Burst

The bright, long-duration type III radio burst emissions due to the escape of flare-accelerated electrons are always associated with long-lasting SEP events (Winter & Ledbetter 2015). We examine the type III radio emissions associated with the eight flares/CMEs observed by the Wind WAVES detector (Bougeret et al. 1995) and STEREO-A WAVES experiment (Bougeret et al. 2008) (see the second row of Figure 3 and the first row of Figure 4). Except for CME 1 and CME 5, which were probably rooted at the back of the Sun for both Wind and STEREO-A, the other six CMEs all have their corresponding type III bursts. It was also reported that the average type III burst duration time at ~ 1 MHz has a positive correlation with the high-energy proton intensity and normally exceeds 20 minutes for strong SEP events (MacDowall et al. 2009). Thus, we check the duration time of the flux density over 4 times (6dB) the background at the frequency of 1.025 MHz for Wind and 1.040 MHz for STEREO-A for each associated type III radio burst as noted in Table 1. We find the type III burst of Flare 2 has the longest duration time, which is 32 minutes in Wind data and 35 minutes in STEREO-A data, and the second-longest one is associated with CME 4 (29 and 28 minutes in STEREO-A and Wind data). The other four events associated with type III radio bursts lasted no more than 10 minutes each. For Flare 8/CME 8, the duration time is only 6 and 4 minutes in STEREO-A and Wind, respectively. All of the above observations suggest that many more particles were released during the solar eruptions of Flare 2/CME 2 than those of Flare 8/CME 8.

2.4. Kinematic Parameters of the CMEs

We use the coronagraph images of the eight CMEs from two perspectives of SOHO and STEREO-A to derive their early kinematic perspectives in the inner heliosphere. The images have to be preprocessed at first and the procedures include despiking with the method by DeForest (2004) and separating dynamic structures by median-filtering pixel by pixel in a temporal sliding window of 12 hr. Then we apply graduated cylindrical shell (GCS) modeling (Thermisien 2011) to fit the CME fronts in coronagraph images of SOHO and STEREO-A almost at the same time (e.g., see Figures 2(a)–(d) for the GCS fitting results of CME 2 and CME 8). Note that the GCS model includes six geometric parameters, in which three are location parameters, including the longitude and latitude of the front nose, and the tilt angle of the flux rope axis γ , while the other three are morphology parameters—the height of the front nose, the half-angle of the flux rope axis δ , and the aspect ratio as the sine of the half-angle of the cone at the flux rope foot κ . Based on a CME's front-nose height of GCS fittings at different times, we calculate its velocity at the front nose v_n by linear fitting.

All of the kinematic parameters derived for the eight CMEs are displayed in Table 1. The longitude and latitude of the CMEs match the associated flares' position on the solar disk very well, especially for the fast CMEs like CME 2 and CME 8. Figures 2(e) and (f) show the GCS fitting results of CME 2 and CME 8 in the coronagraphs. Both CMEs are typically fast

and wide halo- CMEs with longitude closed to 0° away from Earth and their front-nose velocities over 1200 km s^{-1} .

2.5. Magnetic Connection between the CME Front on the Ecliptic Plane and the Observers

The above observation and reconstruction show that CME 1 and CME 5 are backside northwest limb CMEs with no interaction with the ecliptic plane. To estimate the magnetic connectivity for different observers (Earth, STEREO-A, and Mars), we draw the other six CMEs' front cross section on the ecliptic plane with interplanetary magnetic field (IMF) lines as Parker spirals connecting the Sun to each observer. We display the results for CME 2 and CME 8 several hours after the eruption in Figures 2(e) and (f). We find that both CME fronts are well connected to Earth and STEREO-A (under the in situ observed average solar wind speed of 307 and 370 km s^{-1} for CME 2, 566 and 391 km s^{-1} for CME 8 during the relevant time period), shown by the red and green dashed curves as the IMF lines in Figures 2(e) and (f). This suggests that the CME-shock-accelerated SEPs, if any, can easily reach Earth and STEREO-A along the field lines. For Mars, we use the local solar wind velocity predicted by the WSA-ENLIL model simulation result (e.g., Odstrcil & Pizzo 2009) (as 325 km s^{-1} for CME 2 and 461 km s^{-1} for CME 8, both with an estimated error of 100 km s^{-1}) and find the IMF connecting Mars (see the orange dashed-dotted curve within the light yellow uncertainty region in Figures 2(e) and (f)) crossed the flank of CME 2 and deviated the front of CME 8. Under the assumption that particles preferentially travel along the IMF lines (Luhmann et al. 2018), Mars should observe some SEPs accelerated by the CME 2 flank but should hardly see any energetic particles from CME 8. Actually, the in situ observation at Mars does show a clear enhancement of SEPs associated with Flare 2/CME 2 and no SEPs after the onset of Flare 8/CME 8 (2021, private communication with the Mars Science Laboratory/Radiation Assessment Detector (MSL/RAD) team (Hassler et al. 2014) and the Trace Gas Orbiter (TGO)/Liulin-MO team (Semkova et al. 2018), not shown in a figure due to data embargo), supporting the above estimation. We also check the magnetic connectivity of other CME fronts to the three observers as shown in Table 1, with “Y” for a good magnetic connection, “N” for poor connections, and “Y?” for a good connection with weak/no in situ high-energy ($>20 \text{ MeV}$) SEPs. The possible reasons will be discussed in Section 4.

Based on the derived CME front on the ecliptic plane several hours after the eruption, we also roughly predict the CME-driven shock arrival time at Earth or STEREO-A, assuming no more deflection in longitude as shown in Table 1. We only make one failure prediction of CME 4, probably because it had been caught up by CME 8 before its arrival at Earth or STEREO-A as observed by HI2 images.

3. Corresponding In Situ Observations

The third to sixth rows of Figure 3 display the in situ observations from October 28 to November 6 near Earth, each showing the magnetic field magnitude and component, solar wind velocity/proton number density, proton temperature/plasma beta value, and the solar energetic proton flux. These data are recorded by the Wind Magnetic Field Investigation (Lepping et al. 1995), the Solar Wind Experiment (SWE) (Ogilvie et al. 1995), the Three-Dimensional Plasma and

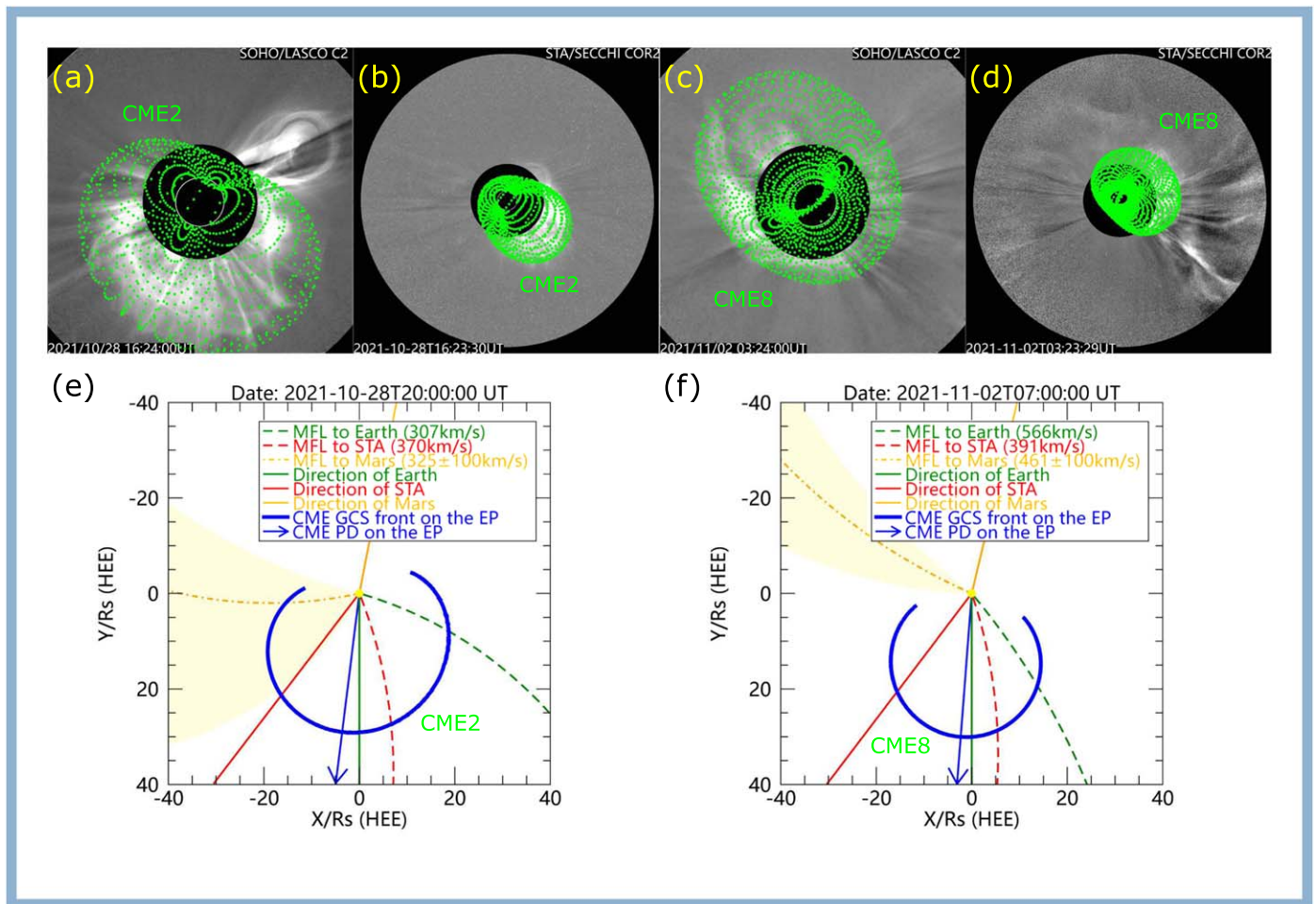


Figure 2. GCS reconstruction of CME 2 and CME 8. (a) and (b) The preprocessed base-difference SOHO/LASCO C2 and STA/COR2 images of CME 2 overlaid with the GCS modeling front as the green dots. (c) and (d) The same as (a) and (b) but for the CME 8. (e) and (f) The GCS front (thick blue solid curve) of CME 2 and CME 8 on the ecliptic plane (EP). The big yellow dot in the center is the Sun. The blue arrow is the nose propagation direction (PD) of the GCS front on the ecliptic plane. We also plot the magnetic field lines (MFL) connecting STEREO-A (red dash curve), Earth (green dashed curve), and Mars (with the orange dashed-dotted curve within the light yellow region as the error range). The corresponding animations of (e) and (f) at different times are available. It covers 5 hr and 25 minutes of the GCS front for CME 2 and CME 8 on the ecliptic plane (from 15:40 UT to 21:05 UT on 2021 October 28 for CME 2, from 02:40 UT to 08:05 UT on 2021 November 2 for CME 8). The video duration is 4 s.

(An animation of this figure is available.)

Energetic Particle Investigation (Lin et al. 1995), and the Energetic Particles: Acceleration, Composition, and Transport investigation (von Roseninge et al. 1995) instruments on board the Wind spacecraft. Right after the flares of CME 2 on October 28, the high-energy (>20 MeV) proton flux started increasing, reached the peak on October 29, and gradually decreased thereafter, lasting for more than 6 days before reaching the pre-event level. At about 9:30 UT on October 31, the shock of CME 2 arrived at Earth. Because CME 2's nose is at latitude S26, Earth passed the northern flank of the shock, which is relatively weak. On November 1, CME4's eruption led to a small re-increase in the high-energy SEPs seen at Earth while no obvious increase is detected after CMEs 3, 6, 7, and 8. At 19:36 UT on November 3, the strong shock of CME 8 arrived. As shown by Figure 3 (third to approximately fifth rows), Earth passed through a thick sheath from November 3 19:36 UT to November 4 10:13 UT (with high proton number density, high proton temperature, and high plasma beta value) and the magnetic cloud from November 4 10:13 UT to November 5 4:24 UT (with a strong magnetic field rotating smoothly, low proton number density, low proton temperature, and low plasma beta value). Interestingly, the high-energy

(>20 MeV) proton flux has a more significant decrease upon the arrival of CME 8. The mechanism is similar to that of a Forbush decrease (Forbush 1937), during which the background cosmic particles can be screened by the CME sheath and magnetic clouds. The difference here is that the background particles are SEPs instead of galactic cosmic radiation filling the near-Earth environment.

The STEREO-A in situ observations by the Plasma and Suprathermal Ion Composition investigation (Galvin et al. 2008) and the In situ Measurements of Particles And CME Transients (Luhmann et al. 2008) experiment are further investigated. The magnetic field magnitude and component, solar wind velocity/proton number density, and solar energetic proton flux are shown in the second, third, and fourth panels of Figure 4, respectively. We observe an even faster SEP flux increase, as compared to that in Figure 3, after the onset of the CME 2 flare. It also reached a higher peak intensity than the flux of high-energy SEPs with similar energies near Earth, probably because the IMF connection of STEREO-A is closer to the nose of the CME 2 shock (see Figure 2(e)). Then, high-energy proton flux fell down slowly, but slightly faster than that at Earth. Despite the data gap in solar

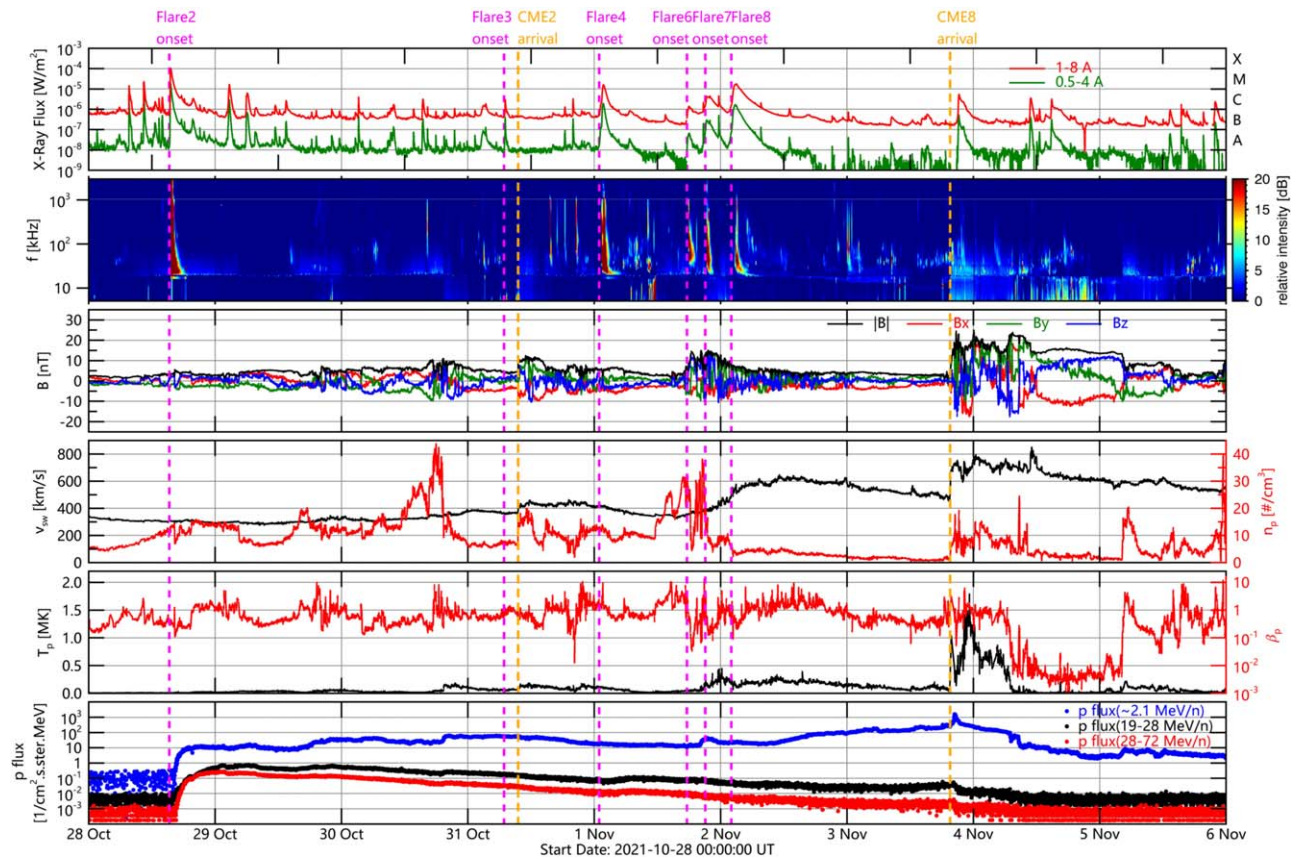


Figure 3. In situ observation near Earth. From top to bottom: X-ray flux observed by GOES-R XRS on board GOES-17, dynamic spectra of Waves radio data, magnetic field magnitude and components in GSE coordinates (X pointing toward the Sun, Y pointing to solar east, and Z normal to the ecliptic), solar wind velocity and proton number density, proton temperature and value of plasma beta, and solar energetic proton flux detected by the Wind spacecraft. The corresponding CME’s flare-onset time (magenta dash line) and CME-driven shock arrival time (orange dash line) are marked as well.

wind velocity and proton number density, the sudden increase in the magnetic field magnitude at 12:22 UT on October 30 indicates the arrival of the CME 2 shock. On November 1, the associated SEP event of CME 4 is weaker than that of CME 2 while CMEs 3, 6, 7, and 8 had almost no influence on the high-energy proton flux. CME 3 arrived at STEREO-A at 9:36 UT on November 3, causing a small bump in 13–21 and lower MeV proton flux and no enhancement for >21 MeV protons. After the strong CME 8 shock arrival at 4:15 UT on November 4, STEREO-A met the large magnetic cloud of CME 8 (from November 4 4:15 UT to November 5 5:18 UT) and the high-energy proton flux decreased to the background level as well. According to the initial propagating parameters of CME 4, we predict its arrival at STEREO-A and Earth after November 4 but the observations only show the arrival of CME 8, which indicates CME 8 caught up with CME 4 on its way to STEREO-A. As Figure 1(c) shows, the remote-sensing observation of STEREO-A HI2 matches this deduction.

At lower energy (several MeV; the blue lines in the bottom panels of Figure 3 and 4), the time profile of solar energetic proton flux is related to the relative position of the observer and the shock front, which can continuously accelerate interplanetary particles to this energy range (Reames 1999). Upon the shock’s arrival, the flux nearly met its peak at Wind but was slightly declining at STEREO-A, indicating that in the longitude of CME 2 and CME 8, it has its shock front more central toward Earth than toward STEREO-A, agreeing with

our previous derivations of CME properties (see Table 1 and Figure 2).

The SEP event related to CME 2 at Mars lasted for no more than 2 days, much less than that at Earth or STEREO-A. There are two reasons: First, Mars stayed at the backside of the Sun to Earth (see Figure 1(b)) and had a weak magnetic connection to the other 7 CMEs (see Table 1). Second, the dose rate as measured by RAD on Mars is mainly induced by primary protons with energies higher than ~ 160 MeV, which could penetrate the Martian atmosphere (Guo et al. 2018).

4. Discussion and Summary

We find eight CMEs from October 28 to November 2 in 2021 and only the second one (CME 2 erupted on October 28) caused strong SEP events at Earth, STEREO-A, and Mars. Based on the analysis of both in situ and remote-sensing observations of the eight CMEs, we discuss if and how each event, especially the eighth one (CME 8 erupted on November 2), corresponds to interplanetary SEPs.

We consider the association of CMEs with SEPs, according to the four main factors concluded by Lario et al. (2020). The first one is magnetic connection. CME 1 and CME 5 had poor magnetic connection to the ecliptic plane leading to no associated SEPs (at energies above 20 MeV) observed at Earth, STEREO-A, and Mars. However, as particle acceleration is an essential factor and pitch-angle scattering or a diffusion process may also favor cross-field transport of particles in the

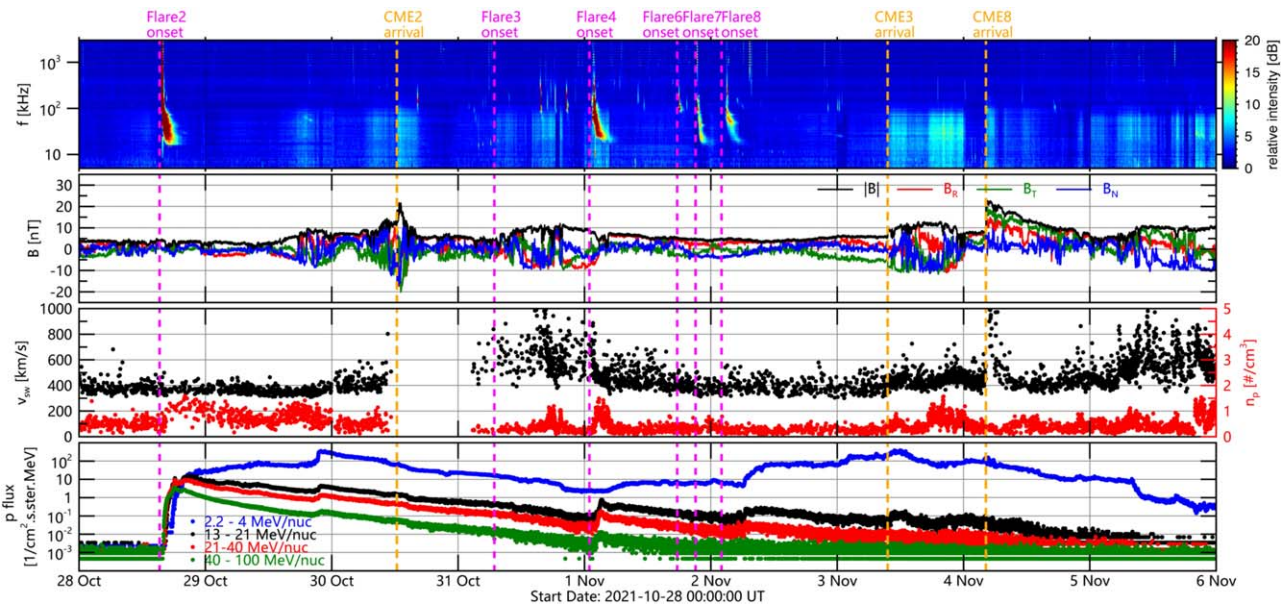


Figure 4. In situ observation by STEREO-A. From top to bottom: dynamic spectra of Waves radio data, magnetic field magnitude and components in RTN coordinates (R, T, and N pointing to radial, transverse and normal directions), solar wind velocity and proton number density (Beacon data, to be processed), and solar energetic proton flux detected by the STEREO-A spacecraft. The corresponding CME’s flare-onset time (magenta dashed line) and CME-driven shock arrival time (orange dashed line) are marked as well.

heliosphere, the IMF connection is not a deterministic factor. We also find some poor SEP signatures under good magnetic connection conditions during CMEs 6, 7, and 8 (see Table 1).

The second one is acceleration efficiency. CME properties like the shock velocity and width can influence the flux of high-energy particles (Kahler et al. 2019). CME 6 is too slow with speeds less than 600 km s^{-1} to drive strong shocks ahead. CME 6 and CME 7 are also too narrow, with edge-on width $\omega_{\text{edge}} = 2 \arcsin \kappa$ less than 60° , to provide a large source region of SEPs.

Another possible reason for the absence of high-energy particles is the lack of pre-CME seed particles. In particular, CME–CME interactions can often happen in the inner heliosphere, and the twin-CME scenario can explain some extremely strong SEP events due to the abundant pre-CME seed particles provided by preceding CMEs (Li et al. 2012; Guo et al. 2018). However, the observations here show the opposite. No other CMEs were observed at the route of CME 2 from its eruption onset to its arrival at 1 au, but CMEs 6, 7, and 8 erupted within ~ 1 day after the eruption of CME 4. Possible CME interactions happened, such as CME 7 and CME 6, CME 8 and CME 7, or CME 8 and CME 4 as indicated in Figure 1(c). CME 7 and CME 8 have good magnetic connectivity in longitude to Earth (see Table 1) and high velocity ($>1000 \text{ km s}^{-1}$) to accelerate SEPs. CME 7 may be too narrow to cause a strong SEP event, but CME 8 is wide enough and the preceding CME 7 and CME 4 can provide enhanced seed population and turbulence level for the CME 8 shock acceleration. However, CME 8 only caused poor/no high-energy SEP signatures at Earth and STEREO-A. One possible explanation is that the preceding CMEs may act as an effective barrier for particle transport and more SEPs may trap inside the pre-CMEs (Kallenrode 2001; Zhuang et al. 2021). However, the observations could not support this explanation as well. CME 8 shock had passed through all the pre-CMEs when it arrived at Earth (see Figures 1(c) and 3), so no barrier effect worked long before the arrival of CME 8 shock, and the

high-energy proton flux should increase to a high level, which did not occur in the observations.

Compared with CME 2, other CMEs like CME 8 have few associated high-energy SEPs, probably because of the lack of as much flare-generated particles as the CME 2 event. Particles accelerated into space during a CME-associated flare can directly contribute to interplanetary SEPs (Cane et al. 2002) and may also act as important seed particles for the (re) acceleration by the CME-driven shock (Lario et al. 2020). Flares 6, 7, and 8 are weaker (according to their class) compared with Flare 2, and the type III radio burst duration time at $\sim 1 \text{ MHz}$ of CMEs 6, 7, and 8 is much less than that of CME 2, which means much less particles released during Flares 6, 7, and 8 than Flare 2, leading to much poorer high-energy SEP signatures.


The SEP signatures in these events suggest two stages of SEP generation. At the first stage within several hours after the CME eruption, it is contributed by flare acceleration and the CME-driven shock acceleration, both in the corona. For CME 2, the first mechanism plays an important role, and the corresponding high-energy particles widely spread into the interplanetary space, which was recorded by observers with magnetic connection to the shock both near its nose (STEREO-A) and at the flank (Wind). At the second stage, the CME-driven shock propagates into interplanetary space and continues accelerating superthermal seed particles therein, although with much lower efficiency resulting in a softer SEP spectrum. Especially for CME 8, which has much more seed particles provided by preceding CMEs (CME 4 and CME 7), the lower-energy proton flux at Earth reached its peak flux upon the shock’s arrival.

Another interesting property of this SEP event at high energy from CME 2 is its long duration. It lasted over 6 days at both Earth and STEREO-A and a few days shorter at Mars. The main reason is the continued injection of high-energy particles to Earth or STEREO-A from other CMEs such as CME 4. Besides, we also find re-increases of energetic protons flux

without corresponding CME eruptions like the two on October 29 and 30 at Earth and the one on October 29 at STEREO-A (see the bottom panels in Figures 3 and 4). They happened along with the ambient solar wind compression region with enhanced magnetic field and proton density variation, and the magnetic focusing effect may play an important role in these flux variations (Wei et al. 2019), which needs to be analyzed specifically in the future.

The STEREO/SECCHI data are produced by a consortium of NRL (USA), RAL (UK), LMSAL (USA), GSFC (USA), MPS (Germany), CSL (Belgium), IOTA (France), and IAS (France). The SOHO/LASCO data are produced by a consortium of the Naval Research Laboratory (USA), Max-Planck-Institut für Aeronomie (Germany), Laboratoire d’Astronomie (France), and the University of Birmingham (UK) and obtained from the Solar and Heliospheric Observatory website (<https://soho.nascom.nasa.gov/>). The SECCHI data presented in this paper were obtained from the STEREO Science Center (<https://stereo-ssc.nascom.nasa.gov/>). The SDO data are produced courtesy of NASA/SDO and the AIA, EVE, and HMI science teams and obtained from the Solar Dynamics Observatory website (<https://sdo.gsfc.nasa.gov/>). The Wind and STEREO-A radio and in situ observation data were obtained from the Space Physics Data Facility (<https://cdaweb.sci.gsfc.nasa.gov/>). The GOES-17 X-ray observation data are obtained from the NOAA website (<https://www.ngdc.noaa.gov/stp/satellite/goes-r.html>). The WSA-ENLIL simulation result was obtained from the NOAA website (<https://www.ngdc.noaa.gov/enlil/>). We acknowledge the use of them. We also acknowledge the support from the National Space Science Data Center, National Science and Technology Infrastructure of China (<http://www.nssdc.ac.cn>). This work is supported by the grants from the Strategic Priority Program of the Chinese Academy of Sciences (XDB41000000 and XDA15017300), the NSFC (41774178, 42174213, and 41761134088), the Informatization Plan of Sciences (grant No. CAS-WX2021PY-0101), and the fundamental research funds for the central universities (WK2080000077).

ORCID iDs

Xiaolei Li  <https://orcid.org/0000-0002-7685-1528>
 Yuming Wang  <https://orcid.org/0000-0002-8887-3919>
 Jingnan Guo  <https://orcid.org/0000-0002-8707-076X>

Shaoyu Lyu  <https://orcid.org/0000-0002-2349-7940>

References

- Bougeret, J. L., Kaiser, M. L., Kellogg, P. J., et al. 1995, *SSRv*, 71, 231
 Bougeret, J. L., Goetz, K., Kaiser, M. L., et al. 2008, *SSRv*, 136, 487
 Brueckner, G. E., Howard, R. A., Koomen, M. J., Korendyke, C. M., & Eyles, C. J. 1995, *SoPh*, 162, 357
 Bučík, R. 2020, *SSRv*, 216, 24
 Cane, H. V., Erickson, W. C., & Prestage, N. P. 2002, *JGRA*, 107, 1315
 Chamberlin, P. C., Woods, T. N., Eparvier, F. G., & Jones, A. R. 2009, *Proc. SPIE*, 7438, 743802
 DeForest, C. E. 2004, *ApJL*, 617, L89
 Eyles, C., Harrison, R., Davis, C. J., et al. 2009, *SoPh*, 254, 387
 Forbush, S. E. 1937, *PhRv*, 51, 1108
 Galvin, A. B., Kistler, L. M., Popecki, M. A., et al. 2008, *SSRv*, 136, 437
 Guo, J., Zeitlin, C., Wimmer-Schweingruber, R. F., et al. 2018, *AJ*, 155, 49
 Hassler, D. M., Zeitlin, C., Wimmer-Schweingruber, R. F., et al. 2014, *Sci*, 343, 1244797
 Howard, R. A., Moses, J. D., Vourlidas, A., et al. 2008, *SSRv*, 136, 67
 Kahler, S. W., Ling, A. G., & Gopalswamy, N. 2019, *SoPh*, 294, 134
 Kahler, S. W., & Vourlidas, A. 2005, *JGRA*, 110, A12S01
 Kallenrode, M. B. 2001, *ICRC (Hamburg)*, 27, 3273
 Kihara, K., Huang, Y., Nishimura, N., et al. 2020, *ApJ*, 900, 75
 Lario, D., Kwon, R. Y., Balmaceda, L., et al. 2020, *ApJ*, 889, 92
 Lemen, J. R., Title, A. M., Akin, D. J., et al. 2012, *SoPh*, 275, 17
 Lepping, R. P., Acuña, M. H., Burlaga, L. F., et al. 1995, *SSRv*, 71, 207
 Li, G., Moore, R., Mewaldt, R. A., Zhao, L., & Labrador, A. W. 2012, *SSRv*, 171, 141
 Lin, R. P., Anderson, K. A., Ashford, S., et al. 1995, *SSRv*, 71, 125
 Luhmann, J. G., Curtis, D. W., Schroeder, P., et al. 2008, *SSRv*, 136, 117
 Luhmann, J. G., Mays, M. L., Odstrcil, D., et al. 2018, in *IAU Symp. 335, Space Weather of the Heliosphere: Processes and Forecasts*, ed. C. Foullon & O. E. Malandraki (Cambridge: Cambridge Univ. Press), 263
 MacDowall, R. J., Richardson, I. G., Hess, R. A., & Thejappa, G. 2009, in *IAU Symp. 257, Universal Heliophysical Processes*, ed. N. Gopalswamy & D. F. Webb (Cambridge: Cambridge Univ. Press), 335
 Odstrcil, D., & Pizzo, V. J. 2009, *SoPh*, 259, 297
 Ogilvie, K. W., Chornay, D. J., Fritzenreiter, R. J., et al. 1995, *SSRv*, 71, 55
 Reames, D. V. 1999, *SSRv*, 90, 413
 Reames, D. V. 2010, *SoPh*, 265, 187
 Reames, D. V. 2013, *SSRv*, 175, 53
 Reames, D. V. 2020, *SSRv*, 216, 20
 Rouillard, A. P., Odstrcil, D., Sheeley, N. R., et al. 2011, *ApJ*, 735, 7
 Semkova, J., Koleva, R., Benghin, V., et al. 2018, *Icar*, 303, 53
 Shen, C., Wang, Y., Ye, P., et al. 2007, *ApJ*, 670, 849
 Thernisien, A. 2011, *ApJS*, 194, 33
 von Rosenvinge, T. T., Barbier, L. M., Karsch, J., et al. 1995, *SSRv*, 71, 155
 Wei, W., Shen, F., Yang, Z., et al. 2019, *JASTP*, 182, 155
 Winter, L. M., & Ledbetter, K. 2015, *ApJ*, 809, 105
 Xie, H., St., Cyr, O. C., Mäkelä, P., & Gopalswamy, N. 2019, *JGRA*, 124, 6384
 Zhuang, B., Lugaz, N., Gou, T., & Ding, L. 2021, *ApJ*, 921, 6
 Zhuang, B., Lugaz, N., & Lario, D. 2022, *ApJ*, 925, 96